

Observation of electron-antineutrino disappearance at Daya Bay

F. P. An,¹ J. Z. Bai,¹ A. B. Balantekin,² H. R. Band,² D. Beavis,³ W. Beriguete,³ M. Bishai,³ S. Blyth,⁴ K. Boddy,⁵ R. L. Brown,³ B. Cai,⁵ G. F. Cao,¹ J. Cao,¹ R. Carr,⁵ W. T. Chan,³ J. F. Chang,¹ Y. Chang,⁴ C. Chasman,³ H. S. Chen,¹ H. Y. Chen,⁶ S. J. Chen,⁷ S. M. Chen,⁸ X. C. Chen,⁹ X. H. Chen,¹ X. S. Chen,¹ Y. Chen,¹⁰ Y. X. Chen,¹¹ J. J. Cherwinka,² M. C. Chu,⁹ J. P. Cummings,¹² Z. Y. Deng,¹ Y. Y. Ding,¹ M. V. Diwan,³ L. Dong,¹ E. Draeger,¹³ X. F. Du,¹ D. A. Dwyer,⁵ W. R. Edwards,¹⁴ S. R. Ely,¹⁵ S. D. Fang,⁷ J. Y. Fu,¹ Z. W. Fu,⁷ L. Q. Ge,¹⁶ V. Ghazikhanian,¹⁷ R. L. Gill,³ J. Goett,¹⁸ M. Gonchar,¹⁹ G. H. Gong,⁸ H. Gong,⁸ Y. A. Gornushkin,¹⁹ L. S. Greenler,² W. Q. Gu,²⁰ M. Y. Guan,¹ X. H. Guo,²¹ R. W. Hackenburg,³ R. L. Hahn,³ S. Hans,³ M. He,¹ Q. He,²² W. S. He,²³ K. M. Heeger,² Y. K. Heng,¹ P. Hinrichs,² T. H. Ho,²³ Y. K. Hor,²⁴ Y. B. Hsiung,²³ B. Z. Hu,⁶ T. Hu,¹ T. Hu,²¹ H. X. Huang,²⁵ H. Z. Huang,¹⁷ P. W. Huang,⁷ X. Huang,²⁶ X. T. Huang,²⁷ P. Huber,²⁴ Z. Isvan,³ D. E. Jaffe,³ S. Jetter,¹ X. L. Ji,¹ X. P. Ji,²⁸ H. J. Jiang,¹⁶ W. Q. Jiang,¹ J. B. Jiao,²⁷ R. A. Johnson,²⁹ L. Kang,³⁰ S. H. Kettell,³ M. Kramer,^{14,31} K. K. Kwan,⁹ M. W. Kwok,⁹ T. Kwok,³² C. Y. Lai,²³ W. C. Lai,¹⁶ W. H. Lai,⁶ K. Lau,²⁶ L. Lebanowski,²⁶ J. Lee,¹⁴ M. K. P. Lee,³² R. Leitner,³³ J. K. C. Leung,³² K. Y. Leung,³² C. A. Lewis,² B. Li,¹ F. Li,¹ G. S. Li,²⁰ J. Li,¹ Q. J. Li,¹ S. F. Li,³⁰ W. D. Li,¹ X. B. Li,¹ X. N. Li,¹ X. Q. Li,²⁸ Y. Li,³⁰ Z. B. Li,³⁴ H. Liang,³⁵ J. Liang,¹ C. J. Lin,¹⁴ G. L. Lin,⁶ S. K. Lin,²⁶ S. X. Lin,³⁰ Y. C. Lin,^{16,9,32,8} J. J. Ling,³ J. M. Link,²⁴ L. Littenberg,³ B. R. Littlejohn,² B. J. Liu,^{9,1,32} C. Liu,¹ D. W. Liu,¹⁵ H. Liu,³² J. C. Liu,¹ J. L. Liu,²⁰ S. Liu,¹⁴ X. Liu,^{1,*} Y. B. Liu,¹ C. Lu,²² H. Q. Lu,¹ A. Luk,⁹ K. B. Luk,^{14,31} T. Luo,¹ X. L. Luo,¹ L. H. Ma,¹ Q. M. Ma,¹ X. B. Ma,¹¹ X. Y. Ma,¹ Y. Q. Ma,¹ B. Mayes,²⁶ K. T. McDonald,²² M. C. McFarlane,² R. D. McKeown,^{5,36} Y. Meng,²⁴ D. Mohapatra,²⁴ J. E. Morgan,²⁴ Y. Nakajima,¹⁴ J. Napolitano,¹⁸ D. Naumov,¹⁹ I. Nemchenok,¹⁹ C. Newsom,²⁶ H. Y. Ngai,³² W. K. Ngai,¹⁵ Y. B. Nie,²⁵ Z. Ning,¹ J. P. Ochoa-Ricoux,¹⁴ D. Oh,⁵ A. Olshevski,¹⁹ A. Pagac,² S. Patton,¹⁴ C. Pearson,³ V. Pec,³³ J. C. Peng,¹⁵ L. E. Piilonen,²⁴ L. Pinsky,²⁶ C. S. J. Pun,³² F. Z. Qi,¹ M. Qi,⁷ X. Qian,⁵ N. Raper,¹⁸ R. Rosero,³ B. Roskovec,³³ X. C. Ruan,²⁵ B. Seilhan,¹³ B. B. Shao,⁸ K. Shih,⁹ H. Steiner,^{14,31} P. Stoler,¹⁸ G. X. Sun,¹ J. L. Sun,³⁷ Y. H. Tam,⁹ H. K. Tanaka,³ X. Tang,¹ H. Themann,³ Y. Torun,¹³ S. Trentalange,¹⁷ O. Tsai,¹⁷ K. V. Tsang,¹⁴ R. H. M. Tsang,⁵ C. Tull,¹⁴ B. Viren,³ S. Virostek,¹⁴ V. Vorobel,³³ C. H. Wang,⁴ L. S. Wang,¹ L. Y. Wang,¹ L. Z. Wang,¹¹ M. Wang,^{27,1} N. Y. Wang,²¹ R. G. Wang,¹ T. Wang,¹ W. Wang,^{36,5} X. Wang,⁸ X. Wang,¹ Y. F. Wang,¹ Z. Wang,^{8,3} Z. Wang,¹ Z. M. Wang,¹ D. M. Webber,² Y. D. Wei,³⁰ L. J. Wen,¹ D. L. Wenman,² K. Whisnant,³⁸ C. G. White,¹³ L. Whitehead,²⁶ C. A. Whitten Jr.,^{17,*} J. Wilhelmi,¹⁸ T. Wise,² H. C. Wong,³² H. L. H. Wong,³¹ J. Wong,⁹ E. T. Worcester,³ F. F. Wu,⁵ Q. Wu,^{27,13} D. M. Xia,¹ S. T. Xiang,³⁵ Q. Xiao,² Z. Z. Xing,¹ G. Xu,²⁶ J. Xu,⁹ J. Xu,²¹ J. L. Xu,¹ W. Xu,¹⁷ Y. Xu,²⁸ T. Xue,⁸ C. G. Yang,¹ L. Yang,³⁰ M. Ye,¹ M. Yeh,³ Y. S. Yeh,⁶ K. Yip,³ B. L. Young,³⁸ Z. Y. Yu,¹ L. Zhan,¹ C. Zhang,³ F. H. Zhang,¹ J. W. Zhang,¹ Q. M. Zhang,¹ K. Zhang,³ Q. X. Zhang,¹⁶ S. H. Zhang,¹ Y. C. Zhang,³⁵ Y. H. Zhang,¹ Y. X. Zhang,³⁷ Z. J. Zhang,³⁰ Z. P. Zhang,³⁵ Z. Y. Zhang,¹ J. Zhao,¹ Q. W. Zhao,¹ Y. B. Zhao,¹ L. Zheng,³⁵ W. L. Zhong,¹⁴ L. Zhou,¹ Z. Y. Zhou,²⁵ H. L. Zhuang,¹ and J. H. Zou¹

(The Daya Bay Collaboration)

¹*Institute of High Energy Physics, Beijing*

²*University of Wisconsin, Madison, WI*

³*Brookhaven National Laboratory, Upton, NY*

⁴*National United University, Miao-Li*

⁵*California Institute of Technology, Pasadena, CA*

⁶*Institute of Physics, National Chiao-Tung University, Hsinchu*

⁷*Nanjing University, Nanjing*

⁸*Department of Engineering Physics, Tsinghua University, Beijing*

⁹*Chinese University of Hong Kong, Hong Kong*

¹⁰*Shenzhen University, Shen Zhen*

¹¹*North China Electric Power University, Beijing*

¹²*Siena College, Loudonville, NY*

¹³*Department of Physics, Illinois Institute of Technology, Chicago, IL*

¹⁴*Lawrence Berkeley National Laboratory, Berkeley, CA*

¹⁵*Department of Physics, University of Illinois at Urbana-Champaign, Urbana, IL*

¹⁶*Chengdu University of Technology, Chengdu*

¹⁷*University of California, Los Angeles, CA*

¹⁸*Department of Physics, Applied Physics, and Astronomy, Rensselaer Polytechnic Institute, Troy, NY*

¹⁹*Joint Institute for Nuclear Research, Dubna, Moscow Region*

²⁰*Shanghai Jiao Tong University, Shanghai*

²¹*Beijing Normal University, Beijing*

²²*Joseph Henry Laboratories, Princeton University, Princeton, NJ*

²³*Department of Physics, National Taiwan University, Taipei*

²⁴*Center for Neutrino Physics, Virginia Tech, Blacksburg, VA*

- ²⁵China Institute of Atomic Energy, Beijing
²⁶Department of Physics, University of Houston, Houston, TX
²⁷Shandong University, Jinan
²⁸School of Physics, Nankai University, Tianjin
²⁹Department of Physics, University of Cincinnati, Cincinnati, OH
³⁰Dongguan Institute of Technology, Dongguan
³¹Department of Physics, University of California, Berkeley, CA
³²Department of Physics, The University of Hong Kong, Pokfulam, Hong Kong
³³Charles University, Faculty of Mathematics and Physics, Prague
³⁴Sun Yat-Sen (Zhongshan) University, Guangzhou
³⁵University of Science and Technology of China, Hefei
³⁶College of William and Mary, Williamsburg, VA
³⁷China Guangdong Nuclear Power Group, Shenzhen
³⁸Iowa State University, Ames, IA
(Dated: November 27, 2024)

The Daya Bay Reactor Neutrino Experiment has measured a non-zero value for the neutrino mixing angle θ_{13} with a significance of 5.2 standard deviations. Antineutrinos from six 2.9 GW_{th} reactors were detected in six antineutrino detectors deployed in two near (flux-weighted baseline 470 m and 576 m) and one far (1648 m) underground experimental halls. With a 43,000 ton-GW_{th}-day livetime exposure in 55 days, 10416 (80376) electron antineutrino candidates were detected at the far hall (near halls). The ratio of the observed to expected number of antineutrinos at the far hall is $R = 0.940 \pm 0.011(\text{stat}) \pm 0.004(\text{syst})$. A rate-only analysis finds $\sin^2 2\theta_{13} = 0.092 \pm 0.016(\text{stat}) \pm 0.005(\text{syst})$ in a three-neutrino framework.

PACS numbers: 14.60.Pq, 29.40.Mc, 28.50.Hw, 13.15.+g

Keywords: neutrino oscillation, neutrino mixing, reactor, Daya Bay

It is well established that the flavor of a neutrino oscillates with time. Neutrino oscillations can be described by the three mixing angles (θ_{12} , θ_{23} , and θ_{13}) and a phase of the Pontecorvo-Maki-Nakagawa-Sakata matrix, and two mass-squared differences (Δm_{32}^2 and Δm_{21}^2) [1, 2]. Of these mixing angles, θ_{13} is the least known. The CHOOZ experiment obtained a 90%-confidence-level upper limit of 0.17 for $\sin^2 2\theta_{13}$ [3]. Recently, results from T2K [4], MINOS [5] and Double Chooz [6] have indicated that θ_{13} could be non-zero. In this paper, we present the observation of a non-zero value for θ_{13} .

For reactor-based experiments, an unambiguous determination of θ_{13} can be extracted via the survival probability of the electron antineutrino $\bar{\nu}_e$ at short distances from the reactors,

$$P_{\text{sur}} \approx 1 - \sin^2 2\theta_{13} \sin^2(1.267 \Delta m_{31}^2 L/E), \quad (1)$$

where $\Delta m_{31}^2 = \Delta m_{32}^2 \pm \Delta m_{21}^2$, E is the $\bar{\nu}_e$ energy in MeV and L is the distance in meters between the $\bar{\nu}_e$ source and the detector (baseline).

The near-far arrangement of antineutrino detectors (ADs), as illustrated in Fig. 1, allows for a relative measurement by comparing the observed $\bar{\nu}_e$ rates at various baselines. With functionally identical ADs, the relative rate is independent of correlated uncertainties and uncorrelated reactor uncertainties are minimized.

A detailed description of the Daya Bay experiment can be found in [7, 8]. Here, only the apparatus relevant to this analysis will be highlighted. The six pressurized water reactors are grouped into three pairs with each pair referred to as a nuclear power plant (NPP). The maximum thermal power of each reactor is 2.9 GW_{th}. Three underground experimental halls (EHs) are connected with horizontal tunnels. Two ADs

are located in EH1 and one in EH2 (the near halls). Three ADs are positioned near the oscillation maximum in the far hall, EH3. The vertical overburden in equivalent meters of water (m.w.e.), the simulated muon rate and average muon energy, and average distance to the reactor pairs are listed in Table I.

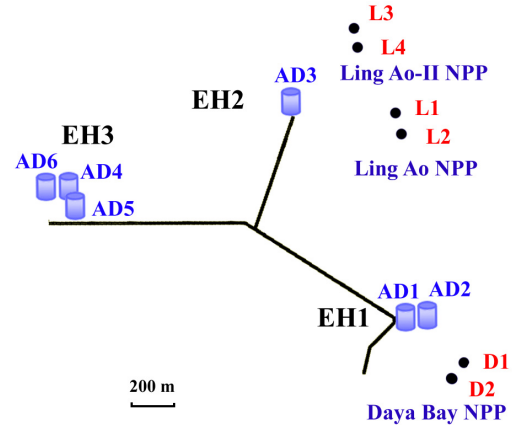


FIG. 1. Layout of the Daya Bay experiment. The dots represent reactors, labeled as D1, D2, L1, L2, L3 and L4. Six ADs, AD1–AD6, are installed in three EHs.

As shown in Fig. 2, the ADs in each EH are shielded with >2.5 m of high-purity water against ambient radiation in all directions. Each water pool is segmented into inner and outer water shields (IWS and OWS) and instrumented with photomultiplier tubes (PMTs) to function as Cherenkov-radiation detectors whose data were used by offline software to remove spallation neutrons and other cosmogenic backgrounds. The

	Overburden	R_μ	E_μ	D1,2	L1,2	L3,4
EH1	250	1.27	57	364	857	1307
EH2	265	0.95	58	1348	480	528
EH3	860	0.056	137	1912	1540	1548

TABLE I. Vertical overburden (m.w.e.), muon rate R_μ (Hz/m²), and average muon energy E_μ (GeV) of the three EHs, and the distances (m) to the reactor pairs.

detection efficiency for long-track muons is $>99.7\%$ [7].

The $\bar{\nu}_e$ is detected via the inverse β -decay (IBD) reaction, $\bar{\nu}_e + p \rightarrow e^+ + n$, in a Gadolinium-doped liquid scintillator (Gd-LS) [9, 10]. The coincidence of the prompt scintillation from the e^+ and the delayed neutron capture on Gd provides a distinctive $\bar{\nu}_e$ signature.

Each AD consists of a cylindrical, 5-m diameter stainless steel vessel (SSV) that houses two nested, UV-transparent acrylic cylindrical vessels. A 3.1-m diameter inner acrylic vessel (IAV) holds 20 t of Gd-LS (target). It is surrounded by a region with 20 t of liquid scintillator (LS) inside a 4-m diameter outer acrylic vessel (OAV). Between the SSV and OAV, 37 t of mineral oil (MO) shields the LS and Gd-LS from radioactivity. IBD interactions are detected by 192 Hamamatsu R5912 PMTs. A black radial shield and specular reflectors are installed on the vertical detector walls and above and below the LS volume, respectively. Gd-LS and LS are prepared and filled into ADs systematically to ensure all ADs are functionally identical [7]. Three automated calibration units (ACUs) mounted on the SSV lid allow for remote deployment of an LED, a ^{68}Ge source, and a combined source of ^{241}Am - ^{13}C and ^{60}Co into the Gd-LS and LS liquid volumes along three vertical axes.

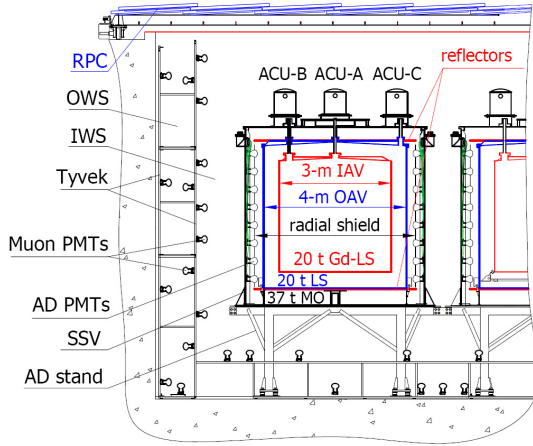


FIG. 2. Schematic diagram of the Daya Bay detectors.

The results are based on data taken from 24 December 2011 to 17 February 2012. A blind analysis strategy was adopted, with the baselines, the thermal power histories of the cores, and the target masses of the ADs hidden until the analy-

ses were frozen. Triggers were formed from the number of PMTs with signals above a ~ 0.25 photoelectron (pe) threshold (NHIT) or the charge-sum of the over-threshold PMTs (ESUM). The AD triggers were $\text{NHIT} > 45$ or $\text{ESUM} \gtrsim 65$ pe. The trigger rate per AD was < 280 Hz with a negligible trigger inefficiency for IBD candidates. The data consist of charge and timing information for each PMT, and were accumulated independently for each detector. To remove systematic effects due to reactor flux fluctuations, only data sets with all detectors in operation were used.

The energy of each trigger in an AD was reconstructed based on the total pe collected by the PMTs. The energy calibration constant, ~ 163 pe/MeV for all ADs and stable throughout the data collection period, was determined by setting the energy peak of the ^{60}Co source deployed at each AD center to 2.506 MeV. Vertex reconstruction was based on center-of-charge (COC), defined as the charge-weighted-mean of the coordinates of all PMTs. The mapping from COC to vertex was done by analytic corrections determined using data collected with ^{60}Co sources deployed at various points within the AD. A vertex-dependent correction to energy ($< 10\%$) and a constant factor (0.988) were applied equally to all ADs to correct for geometrical effects and energy nonlinearity between the ^{60}Co and the neutron capture on Gd ($n\text{Gd}$), determined by the ^{60}Co and Am-C sources at the detector center. An independent energy calibration that utilized the peak of the $n\text{Gd}$ from spallation neutron to set the energy scale and templates derived from Monte Carlo simulations (MC) for vertex reconstruction, gave consistent performance [7]. The energy resolution was $(7.5/\sqrt{E(\text{MeV})} + 0.9)\%$ for all 6 ADs.

IWS and OWS triggers with $\text{NHIT} > 12$ were classified as ‘WS muon candidates’ or μ_{WS} . Events in an AD within $\pm 2 \mu\text{s}$ of a μ_{WS} with energy > 20 MeV and > 2.5 GeV were classified as muons (μ_{AD}) and showering muons (μ_{sh}), respectively, for vetoing purposes. An instrumental background due to spontaneous light emission from a PMT, denoted as a flasher, was rejected efficiently [7].

IBD events were selected with the following criteria: $0.7 < E_p < 12.0$ MeV, $6.0 < E_d < 12.0$ MeV, $1 < \Delta t < 200 \mu\text{s}$, the prompt-delayed pair was vetoed by preceding muons if $t_d - t_{\mu_{\text{WS}}} < 600 \mu\text{s}$, $t_d - t_{\mu_{\text{AD}}} < 1000 \mu\text{s}$ or $t_d - t_{\mu_{\text{sh}}} < 1$ s, and a multiplicity cut that requires no additional > 0.7 MeV trigger in the time range $(t_p - 200 \mu\text{s}, t_d + 200 \mu\text{s})$, where E_p (E_d) is the prompt (delayed) energy and $\Delta t = t_d - t_p$ is the time difference between the prompt and delayed signals. Statistically consistent performance was achieved by an independent analysis that used different energy reconstruction, muon veto, and multiplicity cuts.

The inefficiency of the muon veto for selecting IBD events $(1 - \epsilon_\mu)$ was calculated by integrating the vetoed time of each muon with temporal overlaps taken into account. Inefficiency due to the multiplicity selection $(1 - \epsilon_m)$ was calculated by considering the probability that a random signal occurred near an IBD in time. The average values of $\epsilon_\mu \cdot \epsilon_m$ are given for each AD in Table II.

We considered the following kinds of background: acciden-

	AD1	AD2	AD3	AD4	AD5	AD6
IBD candidates	28935	28975	22466	3528	3436	3452
No-oscillation prediction for IBD	28647	29096	22335	3566.5	3573.0	3535.9
DAQ live time (days)	49.5530		49.4971	48.9473		
Muon veto time (days)	8.7418	8.9109	7.0389	0.8785	0.8800	0.8952
$\epsilon_\mu \cdot \epsilon_m$	0.8019	0.7989	0.8363	0.9547	0.9543	0.9538
Accidentals (per day)	9.82±0.06	9.88±0.06	7.67±0.05	3.29 ±0.03	3.33 ± 0.03	3.12 ±0.03
Fast-neutron (per day)	0.84±0.28	0.84±0.28	0.74±0.44	0.04±0.04	0.04±0.04	0.04±0.04
$^9\text{Li}/^8\text{He}$ (per AD per day)	3.1±1.6		1.8±1.1	0.16±0.11		
Am-C correlated (per AD per day)	0.2±0.2					
$^{13}\text{C}(\alpha, n)^{16}\text{O}$ background (per day)	0.04±0.02	0.04±0.02	0.035±0.02	0.03±0.02	0.03±0.02	0.03±0.02
IBD rate (per day)	714.17±4.58	717.86± 4.60	532.29±3.82	71.78 ± 1.29	69.80±1.28	70.39±1.28

TABLE II. Signal and background summary. The background and IBD rates were corrected for the $\epsilon_\mu \cdot \epsilon_m$ efficiency. The no-oscillation predictions based on reactor flux analyses and detector simulation have been corrected with the best-fit normalization parameter in determining $\sin^2 2\theta_{13}$.

tal correlation of two unrelated signals, β -n decay of $^9\text{Li}/^8\text{He}$ produced by muons in the ADs, fast-neutron backgrounds produced by muons outside the ADs, $^{13}\text{C}(\alpha, n)^{16}\text{O}$ interactions, and correlated events due to the retracted Am-C neutron source in the ACUs. The estimated background rates per AD are summarized in Table II.

The accidental background was determined by measuring the rate of both prompt- and delayed-like signals, and then estimating the probability that two signals randomly satisfied the Δt required for IBD selection. Additional estimates using prompt and delayed candidates separated by more than 1 ms or 2 meters provided consistent results. The uncertainty in the measured accidental rate was dominated by the statistical uncertainty in the rate of delayed candidates.

The rate of correlated background from the β -n cascade of $^9\text{Li}/^8\text{He}$ decays was evaluated from the distribution of the time since the last muon using the known decay times for these isotopes [11]. The $^9\text{Li}/^8\text{He}$ background rate as a function of the muon energy deposited in the AD was estimated by preparing samples with and without detected neutrons 10 μs to 200 μs after the muon. A 50% systematic uncertainty was assigned to account for the extrapolation to zero deposited muon energy.

An energetic neutron entering an AD can form a fast-neutron background by recoiling off a proton before being captured on Gd. By relaxing the $E_p < 12$ MeV criterion in the IBD selection, a flat distribution in E_p was observed up to 100 MeV. Extrapolation into the IBD energy region gave an estimate for the residual fast-neutron background. A similar flat E_p distribution was found in the muon-tagged fast-neutron sample produced by inverting the muon veto cut. Consistent results were obtained by scaling the muon-tagged fast-neutron rate with muon inefficiency, and by MC.

The $^{13}\text{C}(\alpha, n)^{16}\text{O}$ background was determined using MC after estimating the amount of ^{238}U , ^{232}Th , ^{227}Ac , and ^{210}Po in the Gd-LS from their cascade decays, or by fitting their α -particle energy peaks in the data.

A neutron emitted from the 0.5-Hz Am-C neutron source in

an ACU could generate a gamma-ray via inelastic scattering in the SSV before subsequently being captured on Fe/Cr/Mn/Ni. An IBD was mimicked if both gamma-rays from the scattering and capture processes entered the scintillating region. This correlated background was estimated using MC. The normalization was constrained by the measured rate of single delayed-like candidates from this source.

Table III is a summary of the absolute efficiencies and the systematic uncertainties. The uncertainties of the absolute efficiencies are correlated among the ADs. No relative efficiency, except $\epsilon_\mu \cdot \epsilon_m$, was corrected. All differences between the functionally identical ADs were taken as uncorrelated uncertainties.

The spill-in enhancement resulted when neutrons from IBD outside the target drift into the target, and was evaluated using MC. The spill-out deficit ($\sim 2.2\%$) was included in the absolute Gd capture ratio. The Gd capture ratio was studied using Am-C neutron data and MC at the detector center and the spallation neutron data and was determined using IBD MC. Efficiencies associated with the delayed-energy, the prompt-energy, and the capture-time cuts were evaluated with MC. Discussion of the uncertainties in the number of target protons, live time, and the efficiency of the flasher cut can be found in Ref. [7].

Uncorrelated relative uncertainties have been addressed in detail by performing a side-by-side comparison of two ADs [7]. The IBD $n\text{Gd}$ energy peaks for all six ADs were reconstructed to 8.05 ± 0.04 MeV. The relative energy scale between ADs was established by comparing the $n\text{Gd}$ peaks of the IBD- and spallation-neutrons, and alpha-particles in the Gd-LS. Both energy-reconstruction approaches yielded a 0.5% uncorrelated energy-scale uncertainty for all six ADs. The relative uncertainty in efficiency due to the E_d cut was determined to be 0.12% using data. By measuring the difference in the neutron capture time of each AD, from which the Gd-concentration can be calculated, the relative uncertainty in the fraction of neutrons captured on Gd (the Gd capture ratio)

Detector			
	Efficiency	Correlated	Uncorrelated
Target Protons		0.47%	0.03%
Flasher cut	99.98%	0.01%	0.01%
Delayed energy cut	90.9%	0.6%	0.12%
Prompt energy cut	99.88%	0.10%	0.01%
Multiplicity cut		0.02%	<0.01%
Capture time cut	98.6%	0.12%	0.01%
Gd capture ratio	83.8%	0.8%	<0.1%
Spill-in	105.0%	1.5%	0.02%
Livetime	100.0%	0.002%	<0.01%
Combined	78.8%	1.9%	0.2%

Reactor			
	Correlated		Uncorrelated
Energy/fission	0.2%	Power	0.5%
IBD reaction/fission	3%	Fission fraction	0.6%
		Spent fuel	0.3%
Combined	3%	Combined	0.8%

TABLE III. Summary of absolute efficiencies, and correlated and uncorrelated systematic uncertainties.

was found to be $<0.1\%$. All other relative uncertainties were $O(0.01\%)$ and the combined uncertainty was 0.2% . Independent analyses obtained similar results on the background and relative uncertainties.

This analysis was independent of reactor flux models. The $\bar{\nu}_e$ yield per fission [12] was not fixed when determining $\sin^2 2\theta_{13}$. Whether we used the conventional ILL fluxes [13–16] (2.7% uncertainty) or the recently calculated fluxes [17, 18] (3.1% uncertainty) had little impact on the results. The thermal energy released per fission is given in Ref. [19]. Non-equilibrium corrections for long-lived isotopes were applied following Ref. [17]. Contributions from spent fuel [20, 21] ($\sim 0.3\%$) were included as an uncertainty.

Thermal-power data provided by the power plant carry an uncertainty of 0.5% per core [22–24] that we conservatively treat as uncorrelated. The fission fractions were also provided for each fuel cycle as a function of burn-up, with a $\sim 5\%$ uncertainty from validation of the simulation [25, 26]. A DRAGON [27] model was constructed to study the correlation among the fission rates of isotopes. The uncertainties of the fission fraction simulation resulted in a 0.6% uncorrelated uncertainty of the $\bar{\nu}_e$ yield per core. The baselines have been surveyed with GPS and modern theodolites to a precision of 28 mm. The uncertainties in the baseline and the spatial distribution of the fission fractions in the core had a negligible effect to the results. Fig. 3 presents the background-subtracted and efficiency-reactor-corrected IBD rates in the three EHs. Relative reactor flux predictions are shown for comparison.

The $\bar{\nu}_e$ rate in the far hall was predicted with a weighted combination of the two near hall measurements assuming no oscillation. The weights were determined by the thermal

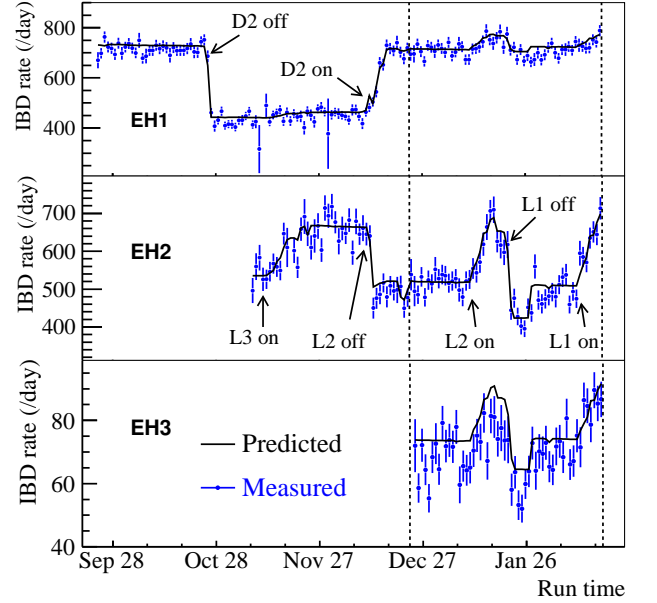


FIG. 3. Daily average measured IBD rates per AD in the three experimental halls as a function of time. Data between the two vertical dashed lines were used in this analysis. The black curves represent no-oscillation predictions based on reactor flux analyses and detector simulation for comparison. The predictions have been corrected with the best-fit normalization parameter in determining $\sin^2 2\theta_{13}$.

power of each reactor and its baseline to each AD. We observed a deficit in the far hall, expressed as a ratio of observed to expected events,

$$R = 0.940 \pm 0.011(\text{stat}) \pm 0.004(\text{syst}).$$

In addition, the residual reactor-related uncertainties were found to be 5% of the uncorrelated uncertainty of a single core.

The value of $\sin^2 2\theta_{13}$ was determined with a χ^2 constructed with pull terms accounting for the correlation of the systematic errors [28],

$$\chi^2 = \sum_{d=1}^6 \frac{[M_d - T_d (1 + \varepsilon + \sum_r \omega_r^d \alpha_r + \varepsilon_d) + \eta_d]^2}{M_d + B_d} + \sum_r \frac{\alpha_r^2}{\sigma_r^2} + \sum_{d=1}^6 \left(\frac{\varepsilon_d^2}{\sigma_d^2} + \frac{\eta_d^2}{\sigma_B^2} \right), \quad (2)$$

where M_d are the measured IBD events of the d -th AD with backgrounds subtracted, B_d is the corresponding background, T_d is the prediction from neutrino flux, MC, and neutrino oscillations [29], ω_r^d is the fraction of IBD contribution of the r -th reactor to the d -th AD determined by baselines and reactor fluxes. The uncertainties are listed in Table III. The uncorrelated reactor uncertainty is σ_r (0.8%), σ_d (0.2%) is the uncorrelated detection uncertainty, and σ_B is the background uncertainty listed in Table II. The corresponding pull parameters are $(\alpha_r, \varepsilon_d, \eta_d)$. The detector- and reactor-related correlated

uncertainties were not included in the analysis; the absolute normalization ε was determined from the fit to the data. The best-fit value is

$$\sin^2 2\theta_{13} = 0.092 \pm 0.016(\text{stat}) \pm 0.005(\text{syst})$$

with a χ^2/NDF of 4.26/4. All best estimates of pull parameters are within its one standard deviation based on the corresponding systematic uncertainties. The no-oscillation hypothesis is excluded at 5.2 standard deviations.

The accidental backgrounds were uncorrelated while the Am-C and (α, n) backgrounds were correlated among ADs. The fast-neutron and ${}^9\text{Li}/{}^8\text{He}$ backgrounds were site-wide correlated. In the worst case where they were correlated in the same hall and uncorrelated among different halls, we found the best-fit value unchanged while the systematic uncertainty increased by 0.001.

Fig. 4 shows the measured numbers of events in each detector, relative to those expected assuming no oscillation. The 6.0% rate deficit is obvious for EH3 in comparison with the other EHs, providing clear evidence of a non-zero θ_{13} . The oscillation survival probability at the best-fit values is given by the smooth curve. The χ^2 versus $\sin^2 2\theta_{13}$ is shown in the inset.

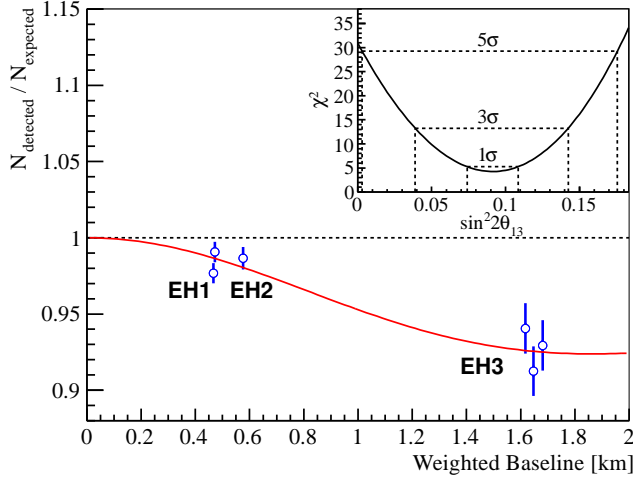


FIG. 4. Ratio of measured versus expected signal in each detector, assuming no oscillation. The error bar is the uncorrelated uncertainty of each AD, including statistical, detector-related, and background-related uncertainties. The expected signal is corrected with the best-fit normalization parameter. Reactor and survey data were used to compute the flux-weighted average baselines. The oscillation survival probability at the best-fit value is given by the smooth curve. The AD4 and AD6 data points are displaced by -30 and +30 m for visual clarity. The χ^2 versus $\sin^2 2\theta_{13}$ is shown in the inset.

The observed $\bar{\nu}_e$ spectrum in the far hall is compared to a prediction based on the near hall measurements in Fig. 5. The disagreement of the spectra provides further evidence of neutrino oscillation. The ratio of the spectra is consistent with the best-fit oscillation solution of $\sin^2 2\theta_{13} = 0.092$ obtained from the rate-only analysis [31].

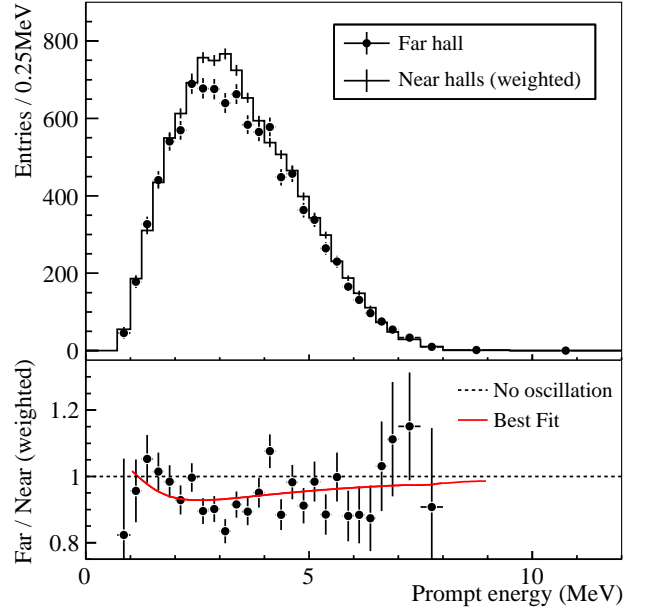


FIG. 5. Top: Measured prompt energy spectrum of the far hall (sum of three ADs) compared with the no-oscillation prediction from the measurements of the two near halls. Spectra were background subtracted. Uncertainties are statistical only. Bottom: The ratio of measured and predicted no-oscillation spectra. The red curve is the best-fit solution with $\sin^2 2\theta_{13} = 0.092$ obtained from the rate-only analysis. The dashed line is the no-oscillation prediction.

In summary, with a 43,000 ton-GW_{th}-day livetime exposure, 10,416 reactor antineutrinos were observed at the far hall. Comparing with the prediction based on the near-hall measurements, a deficit of 6.0% was found. A rate-only analysis yielded $\sin^2 2\theta_{13} = 0.092 \pm 0.016(\text{stat}) \pm 0.005(\text{syst})$. The neutrino mixing angle θ_{13} is non-zero with a significance of 5.2 standard deviations.

The Daya Bay experiment is supported in part by the Ministry of Science and Technology of China, the United States Department of Energy, the Chinese Academy of Sciences, the National Natural Science Foundation of China, the Guangdong provincial government, the Shenzhen municipal government, the China Guangdong Nuclear Power Group, Shanghai Laboratory for Particle Physics and Cosmology, the Research Grants Council of the Hong Kong Special Administrative Region of China, University Development Fund of The University of Hong Kong, the MOE program for Research of Excellence at National Taiwan University, National Chiao-Tung University, and NSC fund support from Taiwan, the U.S. National Science Foundation, the Alfred P. Sloan Foundation, the Ministry of Education, Youth and Sports of the Czech Republic, the Czech Science Foundation, and the Joint Institute of Nuclear Research in Dubna, Russia. We thank Yellow River Engineering Consulting Co., Ltd. and China railway 15th Bureau Group Co., Ltd. for building the underground laboratory. We are grateful for the ongoing cooperation from the China Guangdong Nuclear Power Group and China Light & Power

Company.

* Deceased.

- [1] B. Pontecorvo, Sov. Phys. JETP **6**, 429 (1957) and **26**, 984 (1968).
- [2] Z. Maki, M. Nakagawa, and S. Sakata, Prog. Theor. Phys. **28**, 870 (1962).
- [3] M. Apollonio *et al.* (CHOOZ Collaboration), Phys. Lett. **B466**, 415 (1999); Eur. Phys. J. **C27**, 331 (2003).
- [4] K. Abe *et al.* (T2K Collaboration), Phys. Rev. Lett. **107**, 041801 (2011).
- [5] P. Adamson *et al.* (MINOS Collaboration), Phys. Rev. Lett. **107**, 181802 (2011).
- [6] Y. Abe *et al.* (Double Chooz Collaboration), arXiv:1112.6353 (2012).
- [7] F. P. An *et al.* (Daya Bay Collaboration), arXiv:1202.6181 (2012).
- [8] X. H. Guo *et al.* (Daya Bay Collaboration), Proposal of the Daya Bay experiment, arXiv:hep-ex/0701029 (2007).
- [9] Y. Y. Ding *et al.*, Journal of Rare Earths **25**, 310 (2007); Y. Y. Ding *et al.*, Nucl. Instr. and Meth. **A584**, 238 (2008).
- [10] M. Yeh *et al.*, Nucl. Instr. and Meth. **A578**, 329 (2007).
- [11] L. J. Wen *et al.*, Nucl. Instr. and Meth. **A564**, 471 (2006).
- [12] Y. Declais *et al.*, Phys. Lett. **B338**, 383 (1994).
- [13] W. G. K. Schreckenbach, G. Colvin and F. von Feilitzsch, Phys. Lett. **B160**, 325 (1985).
- [14] A. F. von Feilitzsch and K. Schreckenbach, Phys. Lett. **B118**, 162 (1982).
- [15] A. A. Hahn *et al.*, Phys. Lett. **B218**, 365 (1989).
- [16] P. Vogel, G. K. Schenter, F. M. Mann, and R. E. Schenter, Phys. Rev. **C24**, 1543 (1981).
- [17] T. Mueller *et al.*, Phys. Rev. **C83**, 054615 (2011).
- [18] P. Huber, Phys. Rev. **C84**, 024617 (2011) [Erratum-ibid. **85**, 029901(E) (2012)].
- [19] V. Kopeikin, L. Mikaelyan, and V. Sinev, Phys. Atom. Nucl. **67**, 1892 (2004).
- [20] F. P. An *et al.*, Chin. Phys. **C33**, 711 (2009).
- [21] B. Zhou *et al.*, Chin. Phys. **C36**, 1 (2012).
- [22] J. Cao, proceeding of *Neutrino 2010*, to appear in Nucl. Phys. B Proc. Supp. [arXiv:1101.2266] (2011).
- [23] S. F. E. Tournu *et al.*, EPRI 2001.1001470, Palo Alto, CA (2001).
- [24] C. Xu *et al.*, Chin. J. Nucl. Sci. and Eng. **23**, 26 (2003).
- [25] S. Rauck, SCIENCE V2 nuclear code package - qualification report (Rev A), Framatome ANP Document NFPSD/DC/89, 14 (2004).
- [26] R. Sanchez *et al.*, Nucl. Eng. Tech. **42**, 474 (2010).
- [27] R. R. G. Marleau, A. Hebert, and R. Roy, A User Guide for DRAGON, Report IGE-236 Rev. 1 (2001).
- [28] D. Stump *et al.*, Phys. Rev. **D65**, 014012 (Appendix B) (2001).
- [29] The survival probability used in the χ^2 was $P_{sur} = 1 - \sin^2 2\theta_{13} \sin^2(1.267\Delta m_{31}^2 L/E) - \cos^4 \theta_{13} \sin^2 2\theta_{12} \sin^2(1.267\Delta m_{21}^2 L/E)$ where, $\Delta m_{31}^2 = 2.32 \times 10^{-3} \text{eV}^2$, $\sin^2 2\theta_{12} = 0.861^{+0.026}_{-0.022}$, and $\Delta m_{21}^2 = 7.59^{+0.20}_{-0.21} \times 10^{-5} \text{eV}^2$. The uncertainty in Δm_{31}^2 [30] has not been included in the fit. The fit $\sin^2 2\theta_{13}$ will change by +0.0007 and -0.0004 when Δm_{31}^2 changes by one standard deviation.
- [30] P. Adamson *et al.* (MINOS Collaboration), Phys. Rev. Lett. **106**, 181801 (2011).
- [31] Without correcting for the non-linearity of the detector response, we have performed a preliminary shape analysis that yielded a consistent result for $\sin^2 2\theta_{13}$.